condensed matter

MDPI

Article

The Interplay of Thermal Melting and Pump-Driven Melting of Charge Order: A Two-Temperature Study of the Holstein Model

Debraj Bose [1,2,*], Sankha Subhra Bakshi [1,2,3] and Pinaki Majumdar [4]

[1] Harish-Chandra Research Institute, Chhatnag Road, Jhusi, Allahabad 211019, India
[2] Homi Bhabha National Institute, Training School Complex, Anushakti Nagar, Mumbai 400094, India
[3] Department of Physics, University of Virginia, Charlottesville, VA 22904, USA
[4] School of Arts and Sciences, Ahmedabad University, Navrangpura, Ahmedabad 380009, India
* Correspondence: debrajbose@hri.res.in

Abstract

Charge order driven by electron–phonon coupling is well understood at equilibrium but pump-probe experiments raise a new question: how does this order melt and recover after strong photoexcitation? A pump pulse promotes carriers across the charge-order gap and creates a nonequilibrium high-energy electronic population. In a closed system, the subsequent dynamics are constrained by energy conservation. In an 'open system'—where the system is coupled to a thermal bath at some temperature T_{bath}—there are new fluctuation and dissipation processes at play. One can attempt a computational scheme that incorporates coupling of electrons to a laser pump, the coupling of system phonons to a thermal bath, and the Holstein interaction that couples electrons and phonons. We attempt an approximation where the pump-induced electronic excitations are modeled by a slowly time-varying 'electron temperature', $T_{\mathrm{el}}(t)$, indicative of a quasi-equilibrium electronic state. We solve the problem for different combinations of T_{el} and T_{bath}, probing the order parameter dynamics, the static properties and excitations in the long-time 'quasi-steady state', and establish a 'phase diagram' in terms of bath temperature and electron temperature.

Keywords: Holstein model; charge order; two-temperature model

1. Introduction

Pump-probe experiments provide a direct route to nonequilibrium dynamics in correlated electron systems [1–20]. A short electromagnetic pulse deposits energy primarily in the electronic sector, and the subsequent evolution can be monitored through time-resolved photoemission, optical conductivity, electron diffraction, or X-ray scattering [21–27]. The pumped state is not equivalent to an equilibrium state at some higher temperature, and the electronic distribution, lattice degrees of freedom, and order parameter can evolve on distinct time scales. This separation underlies transient loss of order [3–10], photoinduced or hidden phases [11–14], and large changes in transport and optical response [8,9].

Charge-density-wave and charge-ordered electron–phonon systems are especially useful for studying this physics. Strong electron–phonon coupling can bind carriers to local lattice distortions and form polarons [28–30]. At commensurate filling, these polarons can order into a charge-ordered state with a periodic modulation of both the electronic density and the lattice displacement [31–33]. Pump-probe measurements on such systems often show a rapid suppression of charge order followed by slower recovery. Understanding this

Check for updates

Academic Editor: Amir-Abbas Haghighirad

Received: 23 June 2026
Revised: 8 July 2026
Accepted: 10 July 2026
Published: 17 July 2026

Copyright: © 2026 by the authors. Licensee MDPI, Basel, Switzerland. This article is an open access article distributed under the terms and conditions of the Creative Commons Attribution (CC BY) license.

recovery requires a description that retains both the local amplitude dynamics of the lattice distortion and the real-space growth of ordered domains.

The spinless Holstein model is a minimal setting for this problem, but its nonequilibrium dynamics are challenging even without a bath. After a pump or quench in a closed system, the total energy is conserved and the dynamics cannot be reduced to relaxation toward an externally imposed temperature. Previous studies of Holstein and related charge-order models have shown that the nonequilibrium electronic population strongly affects the lattice response: it can suppress the charge-order amplitude, seed spatial patterns, and slow the return to long-range order [34–38]. Recent machine learning force approaches have also emphasized that the long-time dynamics of charge-density-wave order is limited by the need to follow large-scale domain growth while retaining the electronic contribution to the lattice forces [39–41]. The dynamics are therefore controlled not only by the absorbed energy, but also by how this energy is distributed among excited carriers, lattice distortions, and spatial textures.

The open-system problem, where the system is coupled to a thermal bath, is harder. In a material, both electrons and phonons exchange energy with environmental degrees of freedom. Imagine a classical bath coupled to the system phonons. In that case, one can either (i) retain the environment as part of an enlarged 'system' and use Hamiltonian evolution, or (ii) trace out the environment and bring in a stochastic force and dissipation acting on the system phonons. Neither of these is easy for the large lattices that are needed to probe spatiotemporal dynamics in the driven system.

We use an approximate version of (ii) above to study the simultaneous effect of an external pump and a thermal bath. This is best motivated at strong electron–phonon coupling where the gap is large compared to the phonon frequency or the bath temperature. In this case, relaxation across the gap is bottlenecked. The lattice can then evolve for a long time in the presence of a long-lived excited electronic population. This motivates a two-temperature description in which the electronic sector is characterized by slowly varying temperature $T_{\mathrm{el}}(t)$, while the phonons remain coupled to a bath at T_{bath}. The $T_{\mathrm{el}}(t)$ of course has to be extracted from a microscopic calculation like (i); we discuss this later.

With this approximation the problem looks more familiar —Langevin dynamics becomes a natural tool for the slow phonon sector. The reduction of a system coupled to many bath modes to friction and noise is a standard result of nonequilibrium statistical mechanics and open-system theory [42–47]. In equilibrium, Langevin dynamics provide a controlled description of classical lattice fields coupled to a thermal bath and can be benchmarked against adiabatic Monte Carlo [48,49]. It also gives access to real-space dynamics on lattices large enough to follow domain formation, coarsening, and slow recovery. The central approximation in the present work is to extend this idea to a nonequilibrium two-temperature setting: the phonon coordinates obey Langevin dynamics at T_{bath}, while the electronic contribution to the phonon potential is evaluated using T_{el}.

In this paper, we construct and analyze such a two-temperature Langevin scheme for the half-filled spinless Holstein model. We first motivate the time-dependent electronic temperature from closed-system pump dynamics, where the excited electronic population can be fit to a Fermi distribution. We then use a short-range phonon distortion-dependent expression for the electronic energy, calibrated on the two-site Holstein problem, to avoid repeated diagonalization of the full Hamiltonian during long Langevin simulations. The resulting model allows us to distinguish ordinary thermal melting from pump-induced melting. The former is mainly a loss of spatial coherence between locally distorted regions, while the latter directly suppresses the local distortion amplitude and the associated electronic gap.

The paper is organized as follows. In Section 2 we introduce the microscopic electron-phonon-bath model, derive the stochastic mean-field equations, and explain the approxi-

mations that lead to the two-temperature Langevin dynamics. In Section 3, we present the results in two parts: (i) transient suppression and recovery dynamics and (ii) quasi-steady-state properties. In Section 4, we discuss the limitations of the phenomenological electronic relaxation scheme, and Section 5 summarizes the main conclusions.

2. Model and Method

Our goal is to reduce a microscopic driven electron-phonon-bath problem to a tractable dynamical model for charge-order recovery. The pump creates a nonequilibrium electronic population, while the lattice remains coupled to a thermal environment. A complete treatment would require simultaneous evolution of the driven electrons, quantum phonons, the pump field, and the bath. We instead start from this formulation and use two approximations: the pump-excited electrons are represented by an effective temperature, and the electronic free energy is approximated by a short-range phonon potential.

2.1. Microscopic Electron–Phonon Model

We consider spinless electrons locally coupled to dispersionless phonons on a two-dimensional square lattice. Including the pump field and a phonon bath, the Hamiltonian is

$$\begin{aligned} H &= H_{el} + H_{\text{ph}} + H_{\text{el}-\text{ph}} + H_{\text{bath}} + H_{\text{ph-bath}} \\ &= \sum_{ij} t_{ij}(t)\hat{c}_i^\dagger \hat{c}_j + \sum_i \left(\frac{\hat{p}_i^2}{2M} + \frac{K\hat{x}_i^2}{2} \right) - g\sum_i \hat{n}_i \hat{x}_i \\ &\quad + \sum_\alpha \left(\frac{\hat{P}_\alpha^2}{2M_\alpha} + \frac{K_\alpha \hat{X}_\alpha^2}{2} \right) + \sum_{i\alpha} \kappa_{i\alpha} \hat{x}_i \hat{X}_\alpha. \end{aligned} \tag{1}$$

Here, $\hat{x}_i$ and $\hat{p}_i$ are the local phonon displacement and momentum, M is the phonon mass, K is the bare stiffness, and g is the electron–phonon coupling. The bare phonon frequency is $\Omega_0 = \sqrt{K/M}$. The bath variables $\hat{X}_\alpha$ and $\hat{P}_\alpha$ generate dissipation and thermal noise in the phonon sector through their coupling to the local phonon displacement $\hat{x}_i$ at site i, with coupling strength $\kappa_{i\alpha}$. The filling fraction is set to $\langle n_i \rangle = 1/2$. The pump is included through the Peierls substitution $t_{ij}(t) = t_{ij}^0 \exp\left[i \int_{\mathbf{R}_i}^{\mathbf{R}_j} \mathbf{A}(t) \cdot d\mathbf{l} \right]$, with $\mathbf{E}(t) = -\partial_t \mathbf{A}(t)$. In the absence of the pump, $t_{ij}^0 = -t_{\text{hop}}$ for nearest-neighbour sites and zero otherwise. We use t_{hop} as the unit of energy.

The Heisenberg equations generated by Equation (1) are

$$\begin{aligned} \dot{\hat{x}}_i &= \frac{\hat{p}_i}{M}, \\ \dot{\hat{p}}_i &= -K\hat{x}_i + g\hat{n}_i - \sum_\alpha \kappa_{i\alpha} \hat{X}_\alpha, \\ \dot{\hat{X}}_\alpha &= \frac{\hat{P}_\alpha}{M_\alpha}, \\ \dot{\hat{P}}_\alpha &= -K_\alpha \hat{X}_\alpha - \sum_i \kappa_{i\alpha} \hat{x}_i, \\ \dot{\hat{\rho}}_{ij} &= i[\hat{\rho}, t(t)]_{ij} - i[\hat{\rho}, g\hat{x}_i \delta_{ij}]_{ij}. \end{aligned} \tag{2}$$

Here, $\hat{\rho}_{ij} = \hat{c}_i^\dagger \hat{c}_j$. These equations are exact at the operator level.

2.2. Stochastic Mean-Field Dynamics

The exact equations do not close for expectation values. For example, the equation for $\rho_{ij} = \langle \hat{\rho}_{ij} \rangle$ contains mixed electron–phonon correlators such as $\langle \hat{x}_i \hat{\rho}_{ij} \rangle$. Continuing their equations of motion generates the BBGKY hierarchy. We close this hierarchy at the

mean-field level by using $\langle \hat{x}_i \hat{\rho}_{ij} \rangle \simeq x_i \rho_{ij}$, where $x_i = \langle \hat{x}_i \rangle$ [34]. The lattice coordinates are then treated as classical dynamical variables, while the electronic density matrix evolves quantum mechanically in the instantaneous lattice background.

After this closure, the bath variables can be integrated out. Integrating out the harmonic bath gives a generalized Langevin equation with a memory kernel and fluctuating force; in the Ohmic, Markovian limit, this reduces to local damping and Gaussian white noise satisfying the fluctuation-dissipation relation [42–47]. The resulting stochastic mean-field equations are

$$M\ddot{x}_i = -Kx_i + g\rho_{ii} - \gamma \dot{x}_i + \eta_i(t),$$
$$\dot{\rho}_{ij} = -i[h(\{x_i\}, t), \rho]_{ij}, \tag{3}$$
$$h_{ij}(\{x_i\}, t) = t_{ij}(t) - g x_i \delta_{ij}. \tag{4}$$

The noise satisfies $\langle \eta_i(t) \rangle = 0$ and $\langle \eta_i(t) \eta_j(t') \rangle = 2\gamma T_{\text{bath}} \delta_{ij} \delta(t - t')$. Thus, the phonons exchange energy with a bath at T_{bath}, while the electrons evolve in the time-dependent lattice and pump background.

Equation (4) is a microscopically motivated stochastic mean-field dynamic and is useful for studying the immediate effect of the pump. It is, however, too expensive for the long-time simulations needed here. The electronic density matrix contains $\mathcal{O}(N^2)$ variables, and the adiabatic ratio $\Omega_0 / t_{\text{hop}}$ makes the phonon sector slow compared with the electronic hopping scale. A direct open-system calculation would therefore require a stable high-order scheme for coupled fast ODEs and slow stochastic differential equations over very long times.

In the closed-system limit, $\gamma = 0$, the stochastic force is absent, and Equation (4) reduces to a coupled set of ordinary differential equations. These equations can be solved accurately using, for example, a fourth-order Runge–Kutta algorithm, and they provide the key input for our reduced description: the electronic distribution produced by the pump. For the open-system simulations, we therefore make two simplifications guided by the closed-system dynamics. First, we replace the explicit post-pump electronic evolution by a time-dependent effective electronic temperature $T_{\text{el}}(t)$. Second, we use T_{el} to construct an effective phonon potential, so that the long-time recovery can be studied through classical Langevin dynamics of the lattice alone. We provide a schematic of the working of the closed-system dynamics and the two-temperature open-system dynamics (see below) in Figure 1.

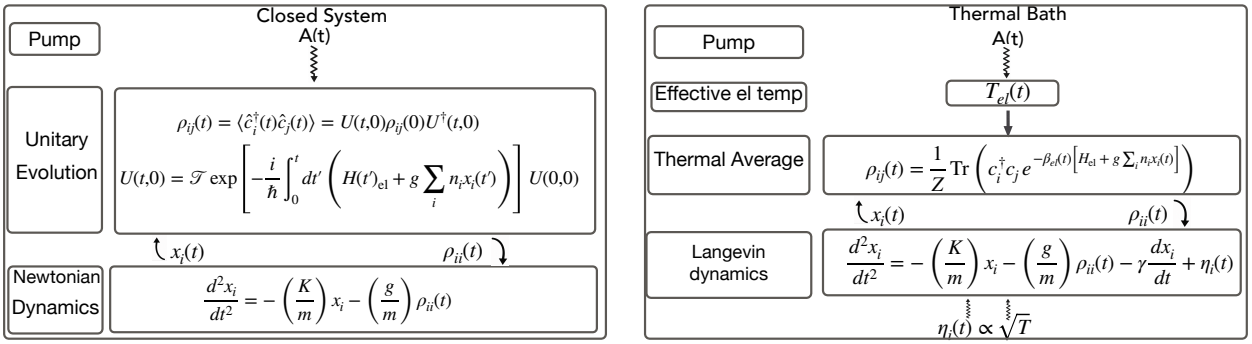


Figure 1. Schematic of two methods. Left: the response of a closed system (no thermal bath) to a pump pulse. The electrons 'see' the pump pulse and the phonon fluctuations, while the phonons see the fluctuating electron density. The system as a whole is energy conserving once the pump pulse passes. Right: the 'two-temperature' version of an open system. Here, the pump generates an effective electron temperature $T_{\text{el}}(t)$, and electronic properties are computed as a *thermal average* at this temperature and in the background of instantaneous phonons. The phonons in turn see the instantaneous electron density. This scheme is valid provided T_{el} and the phonons vary on a timescale much greater than electron hopping.

2.3. Approximations

2.3.1. Electronic-Temperature Quench

The pump primarily excites the electronic sector and creates a nonequilibrium population of high-energy electron-hole excitations. In a full microscopic treatment, one would follow the pulse-driven electronic dynamics, energy redistribution within the electronic sector, and energy transfer to the lattice and bath. Here, we retain only the net effect of this process by introducing a time-dependent electronic temperature $T_{\rm el}(t)$, while the phonons remain coupled to a bath at $T_{\rm bath}$. The post-pump state is therefore described by a two-temperature condition, $T_{\rm el}(t) \neq T_{\rm bath}$. The electronic temperature controls the electronic part of the phonon potential, while $T_{\rm bath}$ controls dissipation and thermal noise.

In principle, one can calibrate the form of $T_{\rm el}(t)$ using the closed-system limit [34]. Setting $\gamma = 0$, we apply an oscillating electric field with carrier frequency $\omega_{\rm pump} = t_{\rm hop}$ and amplitude E_0. The pulse has a Gaussian envelope characterized by $\Omega_{\rm pump} = 3t_{\rm hop}$ and is polarized along the $x + y$ direction, parallel to the system. We extract the electronic population as a function of single-particle energy at each time. This population is fit to a Fermi function,

$$P(\omega, t) \simeq \{\exp[(\omega - \mu(t))/T_{\rm el}(t)] + 1\}^{-1},$$

which defines the effective electronic temperature. Figure 2a shows a representative result, and the inset shows that the instantaneous population is well described by a Fermi form over the relevant energy range.

The extracted electronic temperature relaxes from a high initial value to a lower long-time value. We parametrize this relaxation as

$$T_{\rm el}(t) = T^f_{\rm el} + \left(T^i_{\rm el} - T^f_{\rm el}\right) e^{-t/\tau_{\rm el}}. \tag{5}$$

Here, $T^i_{\rm el}$ is the post-pump value, $T^f_{\rm el}$ is the long-time value, and $\tau_{\rm el}$ is the electronic relaxation time. Repeating the procedure for several pump amplitudes gives the calibration curves in Figure 2b,c. Thus, E_0 fixes the effective temperature-quench parameters $T^i_{\rm el}$, $T^f_{\rm el}$, and $\tau_{\rm el}$.

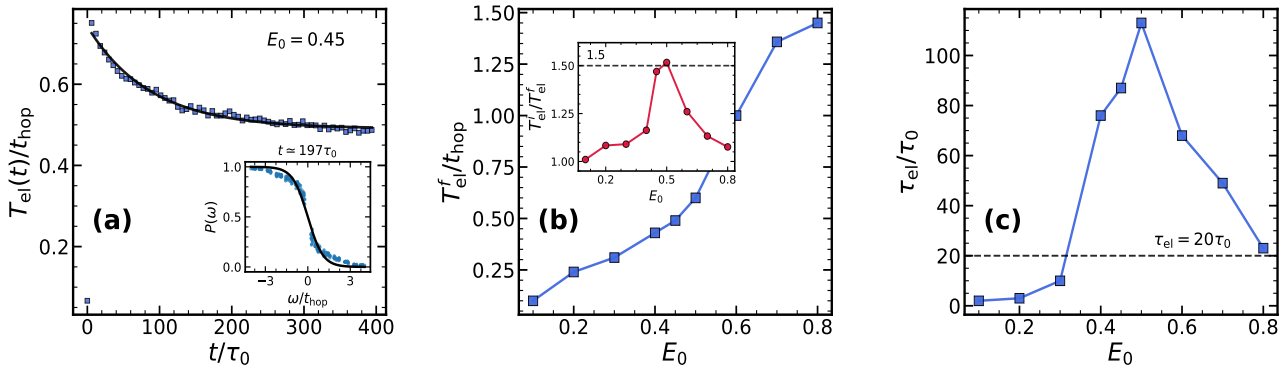


Figure 2. Calibration of the electronic-temperature quench from closed-system pump dynamics. (**a**) $T_{\rm el}(t)$ extracted from the instantaneous electronic population for $E_0 = 0.45$, with an exponential fit. The inset shows a representative Fermi-function fit to $P(\omega)$. (**b**) T^f (and the ratio $T^i_{\rm el}/T^f_{\rm el}$ in the inset) as a function of the pump strength E_0. (**c**) Extracted relaxation time $\tau_{\rm el}$.

In the open-system simulations below, we assume that the same functional form remains a useful phenomenological description. To keep the parameter space small, we fix $T^i_{\rm el}/T^f_{\rm el} = 1.5$ and $\tau_{\rm el} = 20\tau_0$, and use $T^f_{\rm el}$ as the main measure of pump strength.

2.3.2. Effective Short-Range Phonon Model

The remaining task is to compute the force on the lattice distortions without diagonalizing the full electronic Hamiltonian at every Langevin step. We use a short-range effective potential motivated by the two-site Holstein problem. This approximation avoids the $\mathcal{O}(N^3)$ cost of repeated diagonalization. More flexible force models, including machine learning constructions [41], could improve the quantitative accuracy, but the two-site form is sufficient for capturing the strong coupling physics that is central to this work.

For one electron on two sites,

$$H_2^{\mathrm{el}} = -t_{\mathrm{hop}}\left(c_1^\dagger c_2 + c_2^\dagger c_1\right) - g(n_1 x_1 + n_2 x_2). \tag{6}$$

The two eigenvalues are $\lambda_\pm(x_1, x_2) = -gx_+/2 \pm \sqrt{g^2 x_-^2/4 + t_{\mathrm{hop}}^2}$, with $x_+ = x_1 + x_2$ and $x_- = x_1 - x_2$. At electronic temperature T_{el}, the corresponding two-site electronic free energy is

$$F_{\mathrm{el}}(x_1, x_2; T_{\mathrm{el}}) = -T_{\mathrm{el}} \ln\left(e^{-\beta_{\mathrm{el}}\lambda_+} + e^{-\beta_{\mathrm{el}}\lambda_-}\right), \tag{7}$$

where $\beta_{\mathrm{el}} = 1/T_{\mathrm{el}}$. We use this free energy as a nearest-neighbour interaction between lattice distortions. The effective phonon Hamiltonian is

$$H_{\mathrm{ph}}^{\mathrm{eff}} = \sum_i \frac{p_i^2}{2M} + \frac{K}{2}\sum_i x_i^2 + \sum_{\langle ij\rangle} F_{\mathrm{el}}(x_i, x_j; T_{\mathrm{el}}). \tag{8}$$

This form retains the bare local stiffness and includes the short-range electronic tendency toward alternating distortions. Increasing T_{el} weakens the effective ordering tendency and thereby represents the effect of pump-excited carriers.

The final lattice dynamics are then

$$M\ddot{x}_i = -Kx_i - \frac{\partial}{\partial x_i}\sum_{j\in NN(i)} F_{\mathrm{el}}(x_i, x_j; T_{\mathrm{el}}(t)) - \gamma\dot{x}_i + \eta_i(t), \tag{9}$$

with $\langle\eta_i(t)\rangle = 0$ and $\langle\eta_i(t)\eta_j(t')\rangle = 2\gamma T_{\mathrm{bath}}\delta_{ij}\delta(t-t')$. In the simulations, we set $t_{\mathrm{hop}} = 1$, $g = 2$, $K = 1$, and $\Omega_0 = 0.2t_{\mathrm{hop}}$, giving $E_p = g^2/(2K)$ and $\tau_0 = 2\pi/\Omega_0$. Unless stated otherwise, the damping is $\gamma = 0.05$, the lattice size is $L = 30$–50, and observables are averaged over independent noise realizations.

Before applying the two-temperature scheme, we check the equilibrium limit. When $T_{\mathrm{el}} = T_{\mathrm{bath}} = T$, the Langevin distribution generated by Equation (9) should reproduce the thermal properties of the adiabatic Holstein model, at least qualitatively. The charge-order wave vector is $\mathbf{Q} = (\pi, \pi)$, and we define $S_{\mathbf{Q}} = |N^{-1}\sum_i x_i e^{i\mathbf{Q}\cdot\mathbf{R}_i}|^2$.

In the Appendix A, we compare $S_{\mathbf{Q}}$ from the two-site potential with the corresponding Holstein Monte Carlo result.

3. Results

We now present the results of the two-temperature Langevin dynamics. We first discuss transient pump dynamics, including the order parameter, gap, recovery timescales, and real-space domain evolution. Then, we analyze quasi-steady states in the T_{el}–T_{bath} plane.

3.1. Transient Dynamics

We next consider the pump protocol. The electronic temperature relaxes from T_{el}^i to T_{el}^f according to Equation (5), while the phonons remain coupled to a bath at T_{bath}. We use $T_{\mathrm{el}}^f/t_{\mathrm{hop}} = 0.3$, 0.5, and 0.7 as representative weak, intermediate, and strong

pumps. The transient simulations are performed on 50×50 lattices unless stated otherwise. In comparing different parameters, $S_{\mathbf{Q}}(t) = |N^{-1} \sum_i x_i(t) e^{i\mathbf{Q}\cdot\mathbf{R}_i}|^2$ is normalized by its low-temperature equilibrium value.

3.1.1. Time Dependence of the Energy

Before discussing the order-parameter recovery, we first examine the energy flow after the pump. This is useful because the closed and open systems differ most directly in how the absorbed energy is redistributed and removed. In the closed system, the pump injects energy into the electronic sector. After the pulse has passed, the total energy is conserved, although the electronic and phonon parts continue to exchange energy through the Holstein coupling. Thus, the closed-system dynamics describe redistribution of a fixed amount of absorbed energy.

The open-system dynamics are different. The phonons are coupled to a bath at T_{bath} and therefore lose energy through the dissipative part of the Langevin dynamics, while the stochastic force maintains thermal fluctuations at the bath temperature. At the same time, the electronic sector is not allowed to cool self-consistently to the bath. Instead, its effect on the phonon potential is controlled by the imposed electronic temperature $T_{\mathrm{el}}(t)$, which relaxes to the long-time value T_{el}^{f}. The final state is therefore a two-temperature quasi-steady state, not an equilibrium state at T_{bath}.

Figure 3 compares the time dependence of the energy per site relative to the corresponding low-temperature equilibrium value, $\Delta E(t) = E(t) - E_{\mathrm{eq}}$, in the closed and open cases for the same pump strength. In the closed case, the total energy remains constant after the pump, as expected for Hamiltonian dynamics. In the open case, the energy decreases after the pump because the lattice is coupled to the bath. However, the system does not relax back to the low-temperature equilibrium energy set only by T_{bath}. Instead, it approaches a higher quasi-steady value controlled by the residual electronic temperature T_{el}^{f}. In Figure 3b, ΔE_{el} and ΔE_{ph} are measured relative to their respective values in the pre-pump equilibrium state. The phonon energy includes both kinetic and static elastic contributions. Hence, a negative ΔE_{ph} does not necessarily indicate a lower phonon temperature; instead, it reflects the reduction of the static lattice distortion after the pump partially melts the charge order. This energy relaxation illustrates the central assumption of the present approach: the bath cools the phonon sector, while a long-lived hot electronic population continues to weaken the charge-ordering tendency.

3.1.2. Order-Parameter Dynamics

Figure 4 shows the time evolution of the charge-order structure factor for weak and strong pumps. For $T_{\mathrm{el}}^{f}/t_{\mathrm{hop}} = 0.3$, the order parameter is suppressed after the pump but remains finite. The system retains memory of the original checkerboard pattern and recovers smoothly after noise averaging. For $T_{\mathrm{el}}^{f}/t_{\mathrm{hop}} = 0.7$, the suppression is much stronger: $S_{\mathbf{Q}}$ can collapse close to zero, and the recovery becomes slower and more trajectory dependent. The strong-pump case therefore involves reconstruction of charge order from a substantially disordered state, not merely repair of a weakly damaged pattern.

3.1.3. Recovery Timescales

We extract a characteristic recovery time by fitting the noise-averaged trajectories. For weak pumping, where the order parameter remains finite, we use $S_{\mathbf{Q}}(t) = A_d e^{-t/\tau_{\mathrm{decay}}} + S_d + S_r(1 - e^{-t/\tau_{\mathrm{rec}}})$. Here, S_d is the damaged value of the order parameter, S_r is the recovered component, and τ_{rec} is the recovery time. For strong pumping, where the order parameter can approach zero, the delayed growth is better fit by $S_{\mathbf{Q}}(t) = A_d e^{-t/\tau_{\mathrm{decay}}} + S_r \exp[-(\tau_{\mathrm{rec}}/t)^{\alpha}]$, with $\alpha \sim 3 \pm 1$. We use this exponent only as a fitting parameter, not as a claim of universal scaling.

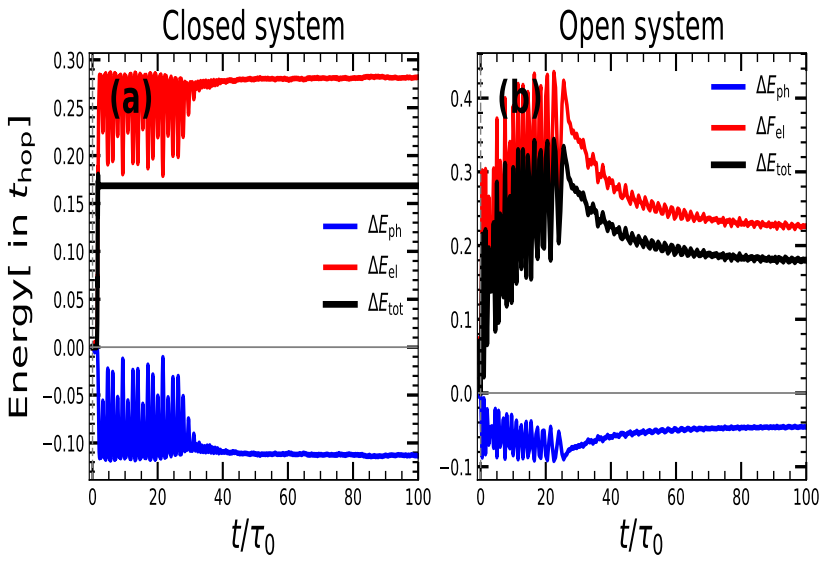


Figure 3. Energy dynamics after the pump for closed and open systems at $E_0 = 0.47$. (**a**) Closed-system energy evolution and (**b**) open-system energy evolution. The open system has $T_{\mathrm{el}}^{f} = 0.5t_{\mathrm{hop}}$ and $T_{\mathrm{bath}} = 0.05t_{\mathrm{hop}}$, and relaxes to a two-temperature quasi-steady state rather than to equilibrium at T_{bath}.

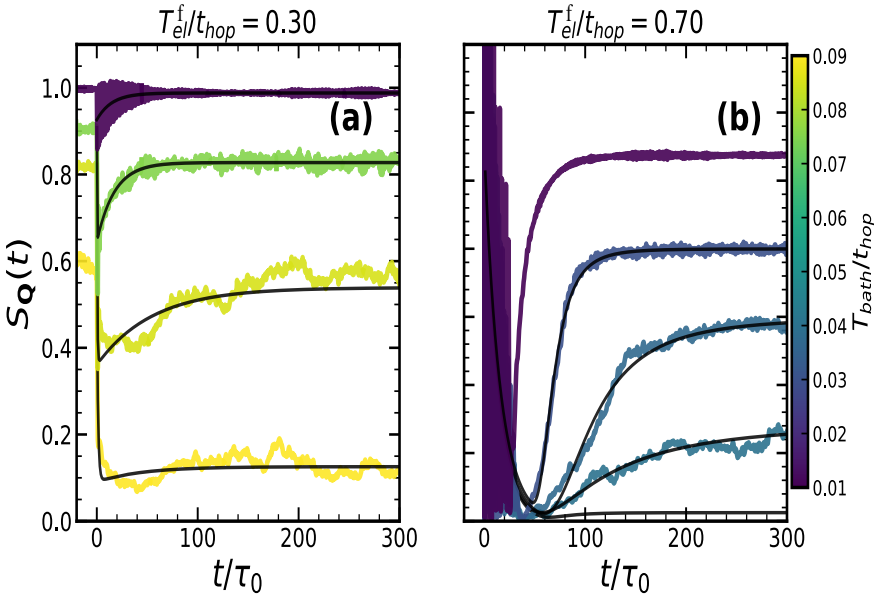


Figure 4. Transient loss and recovery of charge order. (**a**) Weak pumping, $T_{\mathrm{el}}^{f}/t_{\mathrm{hop}} = 0.3$, suppresses $S_{\mathbf{Q}}$ without fully destroying it, (**b**) while strong pumping, $T_{\mathrm{el}}^{f}/t_{\mathrm{hop}} = 0.7$, can nearly extinguish the order. Left panels show individual trajectories and right panels show noise-averaged results.

The extracted timescales are shown in Figure 5. At low bath temperature, τ_{rec} increases with pump strength because larger T_{el}^{f} produces a smaller residual distortion amplitude and a more disrupted domain configuration. As T_{bath} approaches the pump-dependent charge-ordering temperature $T_{\mathrm{bath}}^{\mathrm{CO}}(T_{\mathrm{el}})$, the recovery time grows rapidly. This indicates critical slowing down near the nonequilibrium ordering boundary. The boundary itself shifts to lower T_{bath} with increasing T_{el}, showing that a hot electronic population reduces the bath temperature range over which long-range charge order can survive.

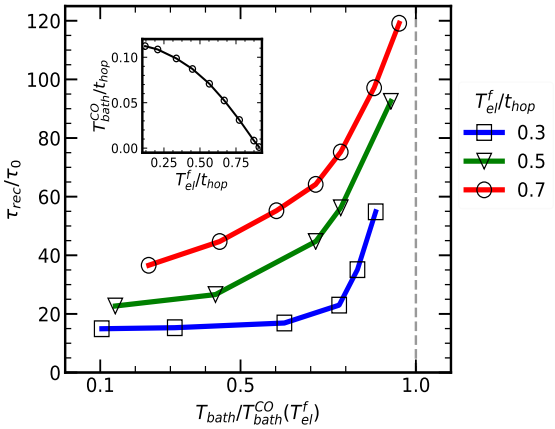


Figure 5. Recovery time τ_{rec} as a function of the bath temperature, normalized by the corresponding charge-ordering transition temperature $T^{\mathrm{CO}}_{\mathrm{bath}}(T^f_{\mathrm{el}})$, for different final electronic temperatures T^f_{el}. The inset shows $T^{\mathrm{CO}}_{\mathrm{bath}}$ as a function of T^f_{el}.

3.1.4. Real-Space Dynamics

The recovery of $S_{\mathbf{Q}}$ involves both local amplitude restoration and domain growth. To visualize this process, we study an intermediate pump, $T^f_{\mathrm{el}}/t_{\mathrm{hop}} = 0.5$, at $T_{\mathrm{bath}}/t_{\mathrm{hop}} = 0.05$. The checkerboard state has two symmetry-related configurations, C and C', differing by a sublattice phase shift. We distinguish them using the local variable $\xi_i = (x_i/x_0 - 1)e^{i\mathbf{Q}\cdot\mathbf{R}_i}$, with $x_0 = g/(2K)$. In an ideal charge-ordered state, ξ_i has opposite signs in the two domains; regions with strongly suppressed distortions correspond to locally melted patches.

Figure 6 shows real-space snapshots, the corresponding momentum-space structure, and the local distortion distribution. The initial state is nearly uniform. Shortly after the pump, the original order is disrupted and domains of both C and C' appear, separated by domain walls and locally melted regions. The Fourier peak at $\mathbf{Q}$ is replaced by broad weight associated with finite domains. At later times, the domains coarsen, one charge-order sector dominates, and the sharp $\mathbf{Q}$ peak is restored.

The bottom row of Figure 6 shows that the local distortion distribution recovers earlier than the global order. Immediately after the pump, $P(x)$ broadens and the two peaks strongly overlap. The bimodality returns before the system is globally ordered, confirming that local polaronic distortions recover before long-range phase coherence.

3.2. Steady-State Results

After the transient, the system reaches a long-lived quasi-steady state specified by the final electronic temperature T^f_{el} and the bath temperature T_{bath}. This state is not in thermal equilibrium unless $T^f_{\mathrm{el}} = T_{\mathrm{bath}}$, but it is stationary on the simulation time scale because the electronic population is held fixed through T^f_{el}. The two temperatures affect charge order in different ways. The bath temperature controls stochastic lattice fluctuations and therefore mainly disorders the phase/domain structure. The electronic temperature enters through the effective phonon potential and directly weakens the local distortion amplitude.

3.2.1. Steady-State Statics

Figure 7 shows the long-time value of $S_{\mathbf{Q}}$ as a function of T_{bath} for several T^f_{el}. The gray curve is the equilibrium result, with a thermal transition near $T_{\mathrm{bath}}/t_{\mathrm{hop}} \simeq 0.12$. For fixed nonzero T^f_{el}, increasing T_{bath} still destroys long-range order, but the transition shifts to lower bath temperature. Thus, a hot electronic population reduces the range of bath temperatures over which charge order can survive. In addition, even at $T_{\mathrm{bath}} = 0$, $S_{\mathbf{Q}}$ decreases with

increasing T_{el}^{f}. This reduction cannot come from thermal phonon fluctuations; it reflects the direct suppression of the local charge-order distortion by the excited electronic population.

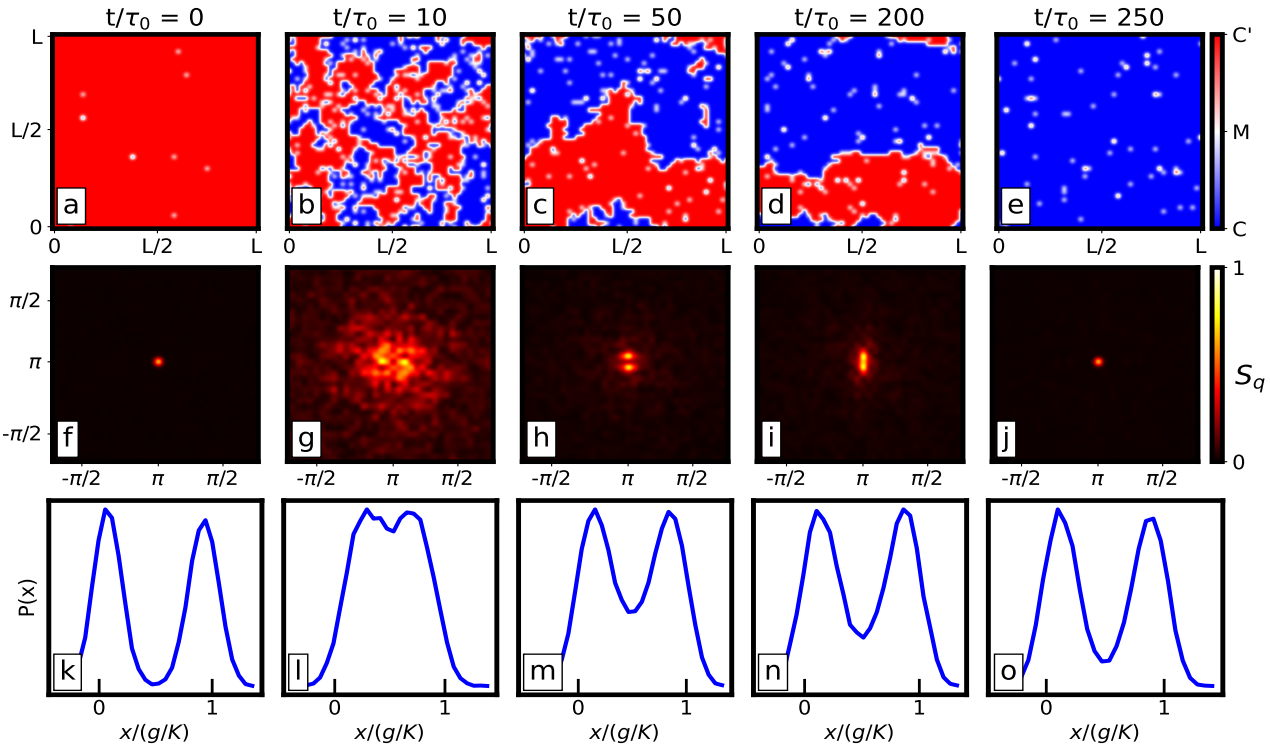


Figure 6. Real-space recovery after an intermediate pump, $T_{\mathrm{el}}^{f}/t_{\mathrm{hop}} = 0.5$, at $T_{\mathrm{bath}}/t_{\mathrm{hop}} = 0.05$. (**a**–**e**) Real-space evolution of charge-order domains. (**f**–**j**) Corresponding momentum-space structure factor. (**k**–**o**) Evolution of the local distortion distribution $P(x)$. The pump creates oppositely phased charge-order domains and locally melted regions; subsequent coarsening restores a dominant checkerboard sector. Momentum-space weight sharpens at $\mathbf{Q}$ only after local bimodality in $P(x)$ has largely recovered.

These results show that the loss of charge order is controlled by two distinct mechanisms: bath-induced loss of spatial coherence and electron-induced reduction of the local distortion amplitude. We now organize these regimes in the full T_{el}^{f}–T_{bath} plane.

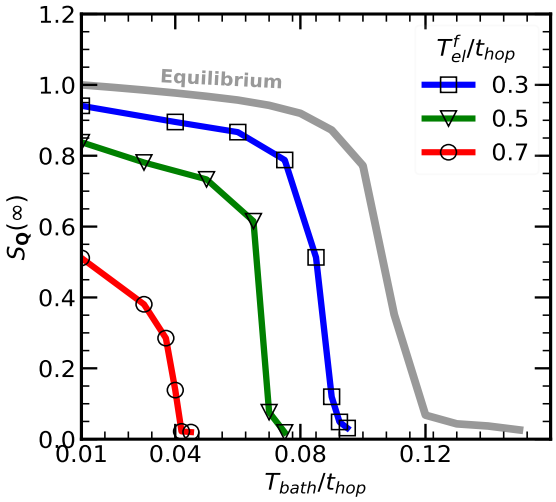


Figure 7. Steady-state charge order. Long-time structure factor $S_{\mathbf{Q}}$ versus bath temperature for different T_{el}^{f}.

3.2.2. Phase Diagram

Figure 8 summarizes the quasi-steady-state behavior. The low-temperature region is charge ordered. Increasing T_{bath} at small T_{el}^{f} destroys long-range order through thermal lattice fluctuations, but local distortions can remain finite. We identify this disordered but locally distorted regime as a polaron liquid. Increasing T_{el}^{f} at low T_{bath} instead suppresses the distortion amplitude itself. At sufficiently large T_{el}^{f}, the system crosses over toward a weakly distorted, Fermi-liquid-like regime.

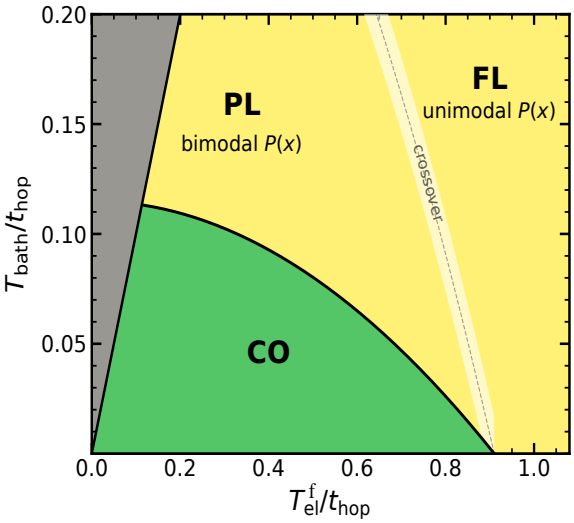


Figure 8. Quasi-steady-state phase diagram in the T_{el}^{f}–T_{bath} plane. The low-temperature CO phase is separated from the disordered regime by the charge-ordering boundary. The shaded band marks the crossover from a polaron liquid with bimodal $P(x)$ to a more homogeneous Fermi-liquid-like regime. The gray region denotes the part of parameter space not accessed by the pump protocol considered here.

The boundary of the CO phase is obtained from the loss of $S_{\mathbf{Q}}$ in the long-time state. The shaded band marks the crossover where the local distortion distribution changes from bimodal to nearly unimodal. Thus, the phase diagram separates two different routes out of the ordered state: a thermal route into a polaronic liquid and an electronic route toward a more homogeneous metallic state.

The diagonal line denotes equilibrium, $T_{\mathrm{el}}^{f} = T_{\mathrm{bath}}$. The gray region with $T_{\mathrm{bath}} > T_{\mathrm{el}}^{f}$ is outside the pump protocol considered here, since after photoexcitation the electronic sector is expected to remain hotter than the bath on the intermediate time scale described by the model.

3.2.3. Phonon Spectrum

The phonon dynamical structure factor gives a frequency-resolved view of the lattice fluctuations. We compute $S(\mathbf{q}, \omega)$ from the space-time Fourier transform of $x_i(t)$.

Figure 9 shows the spectra for several two-temperature conditions. In equilibrium, the phonon mode near $\mathbf{Q} = (\pi, \pi)$ softens and broadens as the charge-ordering transition is approached. The softening indicates a reduced stiffness of the charge-order mode, while the broadening reflects enhanced fluctuations and damping.

For a weak pump, $T_{\mathrm{el}}/t_{\mathrm{hop}} = 0.3$, the same qualitative behavior occurs, but the critical bath temperature is lower. The excited electronic population has already weakened the ordering tendency, so less bath-induced disorder is needed to destroy long-range order. For a strong pump, $T_{\mathrm{el}}/t_{\mathrm{hop}} = 0.7$, the spectrum is substantially modified even at low bath temperature. The mode near $\mathbf{Q}$ is softer and more strongly damped, consistent with proximity to amplitude melting.

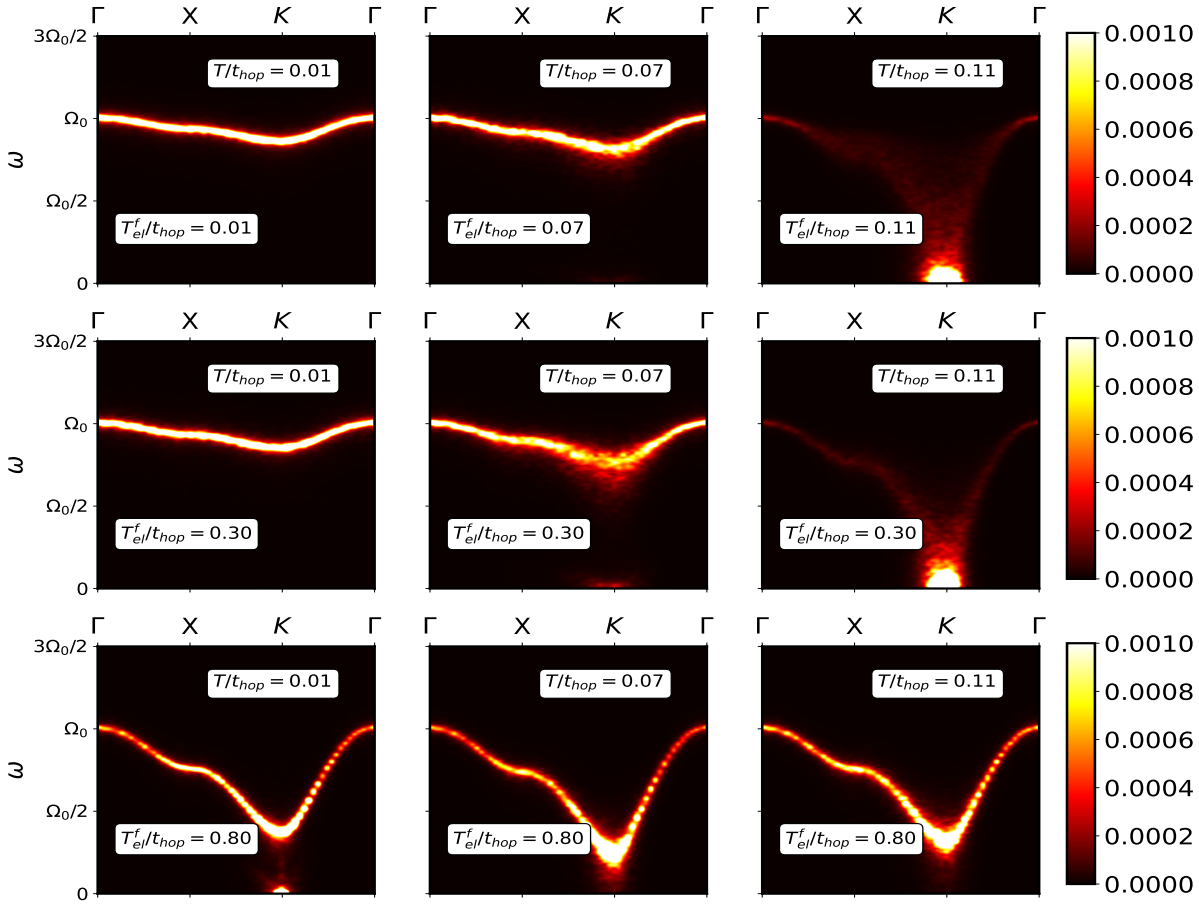


Figure 9. Phonon dynamical structure factor along $\Gamma(0,0)$–$X(\pi,0)$–$K(\pi,\pi)$–$\Gamma(0,0)$. Rows show equilibrium, weak pump, and strong pump conditions. The charge-order mode softens and broadens near the ordering boundary $T_{\mathrm{CO}}^{\mathrm{bath}}(T_{\mathrm{el}}^{f})$ with stronger effects at larger T_{el}^{f}.

3.2.4. Electronic Steady State

We finally characterize the electronic properties of the quasi-steady state. Although the Langevin dynamics are generated using the effective short-range phonon model, the electronic density of states is computed from the full lattice electronic Hamiltonian in the final phonon backgrounds. For each late-time configuration $\{x_i\}$, we diagonalize $h_{ij} = -t_{\mathrm{hop}}\delta_{\langle ij\rangle} - g x_i \delta_{ij}$, and average the resulting spectra over time and independent noise realizations. This gives a direct measure of how the local distortions and domain structure affect the electronic gap. Figure 10 shows the late-time lattice displacement distribution $P(x)$ together with the electronic density of states.

In the charge-ordered regime, $P(x)$ is strongly bimodal, reflecting the two sublattices of the checkerboard state, and the density of states has a clear single-particle gap. Increasing T_{bath} mainly disorders the relative phase of locally distorted regions. As a result, long-range charge order is reduced and in-gap spectral weight appears, but the local distortion distribution can remain bimodal over a substantial range. This is the electronic signature of a polaronic liquid: local lattice distortions survive even after global charge order is weakened. Increasing T_{el} produces a qualitatively different effect. The hot electronic population directly weakens the effective ordering potential, reducing the separation between the two peaks in $P(x)$. The charge-order gap is therefore suppressed even when the bath temperature is low. For sufficiently large T_{el}, the distribution becomes nearly unimodal and the density of states becomes increasingly metallic. Thus, the steady-state electronic spectra support the distinction already suggested by the order parameter and

phase diagram: bath heating mainly destroys spatial coherence between locally distorted regions, whereas electronic heating suppresses the local distortion amplitude itself.

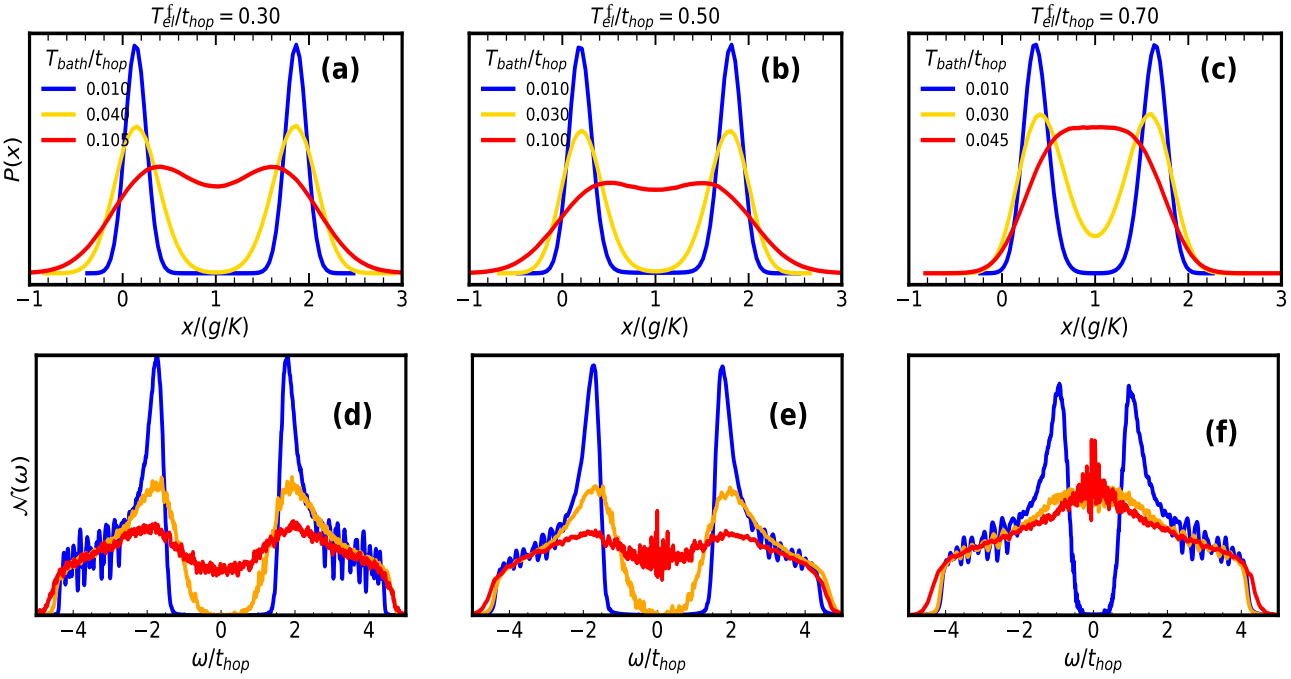


Figure 10. Quasi-steady-state lattice displacement distribution and electronic density of states. (**a**–**c**) The top panels show the distribution of lattice distortions, $P(x)$, for $T_{\mathrm{el}}^f/t_{\mathrm{hop}} = 0.30$, 0.50, and 0.70, respectively. (**d**–**f**) The bottom panels show the corresponding electronic density of states computed from the full lattice electronic Hamiltonian in the final phonon backgrounds. Corresponding electronic density of states $T_{\mathrm{el}}^f/t_{\mathrm{hop}} = 0.30$, 0.50, and 0.70, respectively.

4. Discussion

The main simplification in this work is the treatment of electronic relaxation. The pump-induced electronic population is represented by an effective temperature $T_{\mathrm{el}}(t)$, while the phonons evolve in contact with a bath at T_{bath}. This makes large-lattice, long-time simulations possible, but it is not a consistent microscopic theory of carrier relaxation. The electronic sector does not cool self-consistently by transferring energy to the phonons, and the electronic occupation is not evolved dynamically after $T_{\mathrm{el}}(t)$ has been specified. The parameter T_{el}^f should therefore be interpreted as a long-lived nonequilibrium electronic population, not as a temperature obtained from a complete electron–phonon kinetic theory.

This approximation is most appropriate when the charge-order gap is large compared with the phonon frequency and bath temperature. Accordingly, the portions of the two-temperature phase diagram where the charge-order gap is strongly suppressed or closed should be interpreted as phenomenological regimes indicating loss of order within the model, rather than as regions where the scale-separation argument provides a controlled description of electronic relaxation.

In that regime, relaxation across the gap is slow, and the lattice can evolve for an extended time in a quasi-stationary excited electronic background. The model is therefore intended for an intermediate time window: after the pump has generated high-energy carriers, but before the electronic population has fully recombined and equilibrated with the lattice bath. The two-temperature Langevin scheme should not be viewed as the final stage of thermalization; rather, it isolates the effect of a hot electronic background on charge-order melting and recovery.

A more complete theory would allow $T_{\mathrm{el}}(t)$ to evolve self-consistently. One possible extension is to couple the Langevin dynamics to a rate equation for T_{el}, with a cooling rate that depends on the instantaneous gap, phonon temperature, and distortion amplitude. Such a scheme could capture the feedback in which relaxation is fast when the gap is small but becomes bottlenecked as the gap reopens during recovery. Another extension is a three-temperature model with separate temperatures for electrons, strongly coupled phonons, and the external bath. A still more microscopic approach would evolve the electronic density matrix together with the phonons and bath, but this is much more demanding for the sizes and times needed to follow domain coarsening.

These extensions would mainly affect the late-time return to full equilibrium. In the present work, the long-time state is a quasi-steady state at fixed T_{el} and T_{bath}. If the electronic temperature were allowed to relax to the bath temperature, the system would eventually move toward the equilibrium line of the two-temperature phase diagram. The route to that line would depend on the electronic cooling time. Slow cooling allows the system to remain in the two-temperature regime long enough for hot carriers to suppress local distortions and delay recovery. Fast cooling would make the dynamics closer to ordinary thermal recovery controlled by the phonon bath. Thus, the missing electronic relaxation does not remove the usefulness of the two-temperature phase diagram, but it determines how a real pump-probe trajectory moves through it.

5. Conclusions

We have introduced a two-temperature Langevin framework for the melting and recovery of charge order in the half-filled spinless Holstein model. The electronic sector is represented by an effective temperature T_{el}, while the phonons evolve through Langevin dynamics at T_{bath}. This provides a tractable semiclassical approach to large lattices and long times, where recovery involves both local distortion dynamics and collective domain growth.

The transient simulations show clear loss and recovery of charge order. Weak pumping suppresses the order parameter without fully destroying it, leading to relatively smooth recovery. Strong pumping can nearly extinguish $S_{\mathbf{Q}}$, after which recovery is slower and more collective. The recovery time increases with pump strength and grows rapidly near the pump-dependent charge-ordering boundary.

The quasi-steady-state phase diagram summarizes the interplay of electronic and bath temperatures. At low T_{el} and low T_{bath}, the system is charge ordered. Thermal fluctuations produce a disordered polaronic liquid in which local distortions remain, while strong electronic heating suppresses the distortion amplitude and drives a crossover to a weakly distorted metallic regime. The phonon dynamical structure factor and electronic density of states support this picture: the charge-order phonon mode softens and broadens near the ordering boundary, and the electronic gap is progressively filled and suppressed as T_{el} increases.

The main limitation is that electronic relaxation is treated phenomenologically. The effective electronic temperature is not obtained from a self-consistent energy-transfer calculation, so the final two-temperature state should be interpreted as a long-lived intermediate regime rather than the ultimate thermal equilibrium state. Future work should incorporate self-consistent electronic cooling, a three-temperature description, or direct stochastic mean-field simulations of coupled electron–phonon–bath dynamics. Such extensions would determine how real pump-probe trajectories move through the two-temperature phase diagram and eventually return to equilibrium.

https://doi.org/10.3390/condmat11030027

Author Contributions: Conceptualization, D.B., S.S.B. and P.M.; Methodology, D.B., S.S.B. and P.M.; Software, D.B., S.S.B. and P.M.; Validation, D.B., S.S.B. and P.M.; Formal analysis, D.B., S.S.B. and P.M.; Investigation, D.B., S.S.B. and P.M.; Resources, D.B., S.S.B. and P.M.; Data curation, D.B. and S.S.B.; Writing—original draft, D.B., S.S.B. and P.M.; Writing—review & editing, D.B., S.S.B. and P.M.; Visualization, S.S.B. and P.M.; Supervision, S.S.B. and P.M.; Project administration, S.S.B. and P.M. All authors have read and agreed to the published version of the manuscript.

Funding: This research received no external funding. S.S.B. was partially supported by the US Department of Energy, Basic Energy Sciences under Contract No. DE-SC0020330.

Data Availability Statement: The original contributions presented in this study are included in the article. Further inquiries can be directed to the corresponding author.

Acknowledgments: The authors acknowledge use of the HPC clusters at HRI.

Conflicts of Interest: The authors declare no conflict of interest.

Appendix A. Benchmarking the Two-Site Approximation

The effective model captures the thermal charge-ordering scale reasonably well. Its main quantitative error is a larger low-temperature value of $S_{\mathbf{Q}}$, caused by the tendency of the two-site potential to overestimate the local distortion amplitude. For the present purpose, the important point is that long-range charge order is lost in the same temperature range in the two calculations.

The local distortion distribution provides a more microscopic test. Figure A1 shows P(x) deep in the ordered phase, in the intermediate anharmonic regime, and close to the equilibrium transition. Both methods show a clear bimodal distribution at low temperature, corresponding to the two sublattices of the checkerboard charge order. With increasing temperature, the peaks broaden and overlap, but the distribution remains bimodal near the transition.

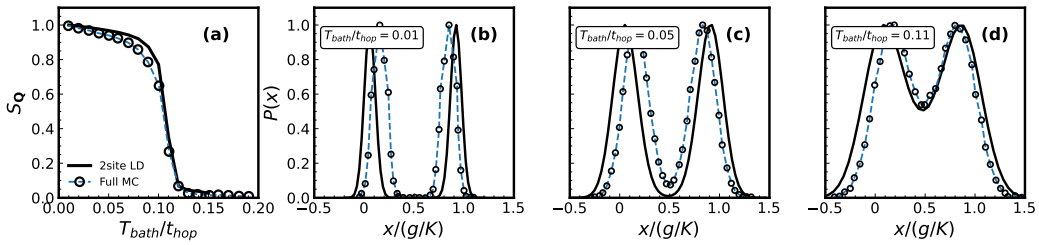


Figure A1. Equilibrium benchmarks of the effective two-site model. (**a**) Normalized charge-order structure factor $S_{\mathbf{Q}}$ as a function of temperature, compared with adiabatic Holstein Monte Carlo results. (**b**–**d**) Equilibrium distributions of local distortions $P(x)$ at representative temperatures. Both the full Holstein model and the effective Langevin model show a bimodal distribution at low and intermediate temperatures, with local distortions persisting close to T_{CO}. This indicates that the loss of charge order near the transition is mainly associated with phase/domain melting rather than an immediate collapse of the local distortion amplitude.

This behavior is characteristic of strong-coupling charge-order melting. Local distortions remain finite near and above the ordering temperature, while long-range coherence between charge-ordered regions is lost. Equilibrium melting is therefore primarily phase/domain driven. This benchmark sets the reference for the nonequilibrium results, where increasing T_{el} produces a more direct suppression of the distortion amplitude.

References

1. Bloch, J.; Cavalleri, A.; Galitski, V.; Hafezi, M.; Rubio, A. Strongly correlated electron–photon systems. *Nature* **2022**, *606*, 41–48. [CrossRef] [PubMed]
2. Beaurepaire, E.; Merle, J.C.; Daunois, A.; Bigot, J.Y. Ultrafast Spin Dynamics in Ferromagnetic Nickel. *Phys. Rev. Lett.* **1996**, *76*, 4250. [CrossRef] [PubMed]

3. Carpene, E.; Mancini, E.; Dallera, C.; Brenna, M.; Puppin, E.; De Silvestri, S. Dynamics of electron-magnon interaction and ultrafast demagnetization in thin iron films. *Phys. Rev. B* **2008**, *78*, 174422. [CrossRef]
4. Beaud, P.; Johnson, S.L.; Vorobeva, E.; Staub, U.; De Souza, R.A.; Milne, C.J.; Jia, Q.X.; Ingold, G. Ultrafast Structural Phase Transition Driven by Photoinduced Melting of Charge and Orbital Order. *Phys. Rev. Lett.* **2009**, *103*, 155702. [CrossRef] [PubMed]
5. Fiebig, M.; Miyano, K.; Tomioka, Y.; Tokura, Y. Sub-picosecond photo-induced melting of a charge-ordered state in a perovskite manganite. *Appl. Phys. B* **2000**, *71*, 211–215. [CrossRef]
6. Matsuzaki, H.; Uemura, H.; Matsubara, M.; Kimura, T.; Tokura, Y.; Okamoto, H. Detecting charge and lattice dynamics in photoinduced charge-order melting in perovskite-type manganites using a 30-femtosecond time resolution. *Phys. Rev. B* **2009**, *79*, 235131. [CrossRef]
7. Chávez-Cervantes, M.; Topp, G.E.; Aeschlimann, S.; Krause, R.; Sato, S.A.; Sentef, M.A.; Gierz, I. Charge Density Wave Melting in One-Dimensional Wires with Femtosecond Subgap Excitation. *Phys. Rev. Lett.* **2019**, *123*, 036405. [CrossRef] [PubMed]
8. Iwai, S.; Ono, M.; Maeda, A.; Matsuzaki, H.; Kishida, H.; Okamoto, H.; Tokura, Y. Ultrafast Optical Switching to a Metallic State by Photoinduced Mott Transition in a Halogen-Bridged Nickel-Chain Compound. *Phys. Rev. Lett.* **2003**, *91*, 057401. [CrossRef] [PubMed]
9. Okamoto, H.; Matsuzaki, H.; Wakabayashi, T.; Takahashi, Y.; Hasegawa, T. Photoinduced Metallic State Mediated by Spin-Charge Separation in a One-Dimensional Organic Mott Insulator. *Phys. Rev. Lett.* **2007**, *98*, 037401. [CrossRef] [PubMed]
10. Cho, D.; Cheon, S.; Kim, K.; Lee, S.H.; Cho, Y.H.; Cheong, S.W.; Yeom, H.W. Nanoscale manipulation of the Mott insulating state coupled to charge order in 1T-TaS_2. *Nat. Commun.* **2015**, *7*, 10453. [CrossRef] [PubMed]
11. Ichikawa, H.; Nozawa, S.; Sato, T.; Tomita, A.; Ichiyanagi, K.; Chollet, M.; Guerin, L.; Dean, N.; Cavalleri, A.; Adachi, S.; et al. Transient photoinduced 'hidden' phase in a manganite. *Nat. Mater.* **2011**, *10*, 101–105. [CrossRef] [PubMed]
12. Liu, Q.M.; Wu, D.; Li, Z.A.; Shi, L.Y.; Wang, Z.X.; Zhang, S.J.; Lin, T.; Hu, T.C.; Tian, H.F.; Li, J.Q.; et al. Photoinduced multistage phase transitions in Ta_2NiSe_5. *Nat. Commun.* **2021**, *12*, 2050. [CrossRef] [PubMed]
13. Budden, M.; Gebert, T.; Buzzi, M.; Jotzu, G.; Wang, E.; Matsuyama, T.; Meier, G.; Laplace, Y.; Pontiroli, D.; Riccò, M.; et al. Evidence for metastable photo-induced superconductivity in K_3C_{60}. *Nat. Phys.* **2021**, *17*, 611–618. [CrossRef]
14. Fausti, D.; Tobey, R.I.; Dean, N.; Kaiser, S.; Dienst, A.; Hoffmann, M.C.; Pyon, S.; Takayama, T.; Takagi, H.; Cavalleri, A. Light-Induced Superconductivity in a Stripe-Ordered Cuprate. *Science* **2011**, *331*, 189–191. [CrossRef] [PubMed]
15. Zhang, Y.; Shi, X.; You, W.; Tao, Z.; Zhong, Y.; Kabeer, F.; Maldonado, P.; Oppeneer, P.; Bauer, M.; Rossnagel, K.; et al. Coherent modulation of the electron temperature and electron-phonon couplings in a 2D material. *Proc. Natl. Acad. Sci. USA* **2020**, *117*, 8788–8793. [CrossRef] [PubMed]
16. Maklar, J.; Windsor, Y.W.; Nicholson, C.W.; Puppin, M.; Walmsley, P.; Esposito, V.; Porer, M.; Rittmann, J.; Leuenberger, D.; Kubli, M.; et al. Nonequilibrium charge-density-wave order beyond the thermal limit. *Nat. Commun.* **2021**, *12*, 2499. [CrossRef] [PubMed]
17. Schmitt, F.; Kirchmann, P.; Bovensiepen, U.; Moore, R.; Chu, J.; Lu, D.; Rettig, L.; Wolf, M.; Fisher, I.; Shen, Z. Ultrafast electron dynamics in the charge density wave material $TbTe_3$. *New J. Phys.* **2011**, *13*, 063022. [CrossRef]
18. Rettig, L.; Chu, J.; Fisher, I.; Bovensiepen, U.; Wolf, M. Coherent dynamics of the charge density wave gap in tritellurides. *Phys. Rev. Lett.* **2014**, *114*, 067402. [CrossRef] [PubMed]
19. Han, T.; Zhou, F.; Malliakas, C.; Duxbury, P.; Mahanti, S.; Kanatzidis, M.; Ruan, C.Y. Exploration of metastability and hidden phases in correlated electron crystals visualized by femtosecond optical doping and electron crystallography. *Sci. Adv.* **2015**, *1*, e1400173. [CrossRef] [PubMed]
20. Hellmann, S.; Beye, M.; Sohrt, C.; Rohwer, T.; Sorgenfrei, F.; Redlin, H.; Kallane, M.; Marczynski-Buhlow, M.; Hennies, F.; Bauer, M.; et al. Ultrafast Melting of a Charge-Density Wave in the Mott Insulator 1T-TaS_2. *Phys. Rev. Lett.* **2010**, *105*, 187401. [CrossRef] [PubMed]
21. Carpene, E.; Mancini, E.; Dallera, C.; Ghiringhelli, G.; Manzoni, C.; Cerullo, G.; Silvestri, S.D. A versatile apparatus for time-resolved photoemission spectroscopy via femtosecond pump-probe experiments. *Rev. Sci. Instrum.* **2009**, *80*, 055101. [CrossRef] [PubMed]
22. Sobota, J.; He, Y.; Shen, Z. Angle-resolved photoemission studies of quantum materials. *Rev. Mod. Phys.* **2021**, *93*, 025006. [CrossRef]
23. Eich, S.; Stange, A.; Carr, A.; Urbancic, J.; Popmintchev, T.; Wiesenmayer, M.; Jansen, K.; Ruffing, A.; Jakobs, S.; Rohwer, T.; et al. Time- and angle-resolved photoemission spectroscopy with optimized high-harmonic pulses using frequency-doubled Ti:Sapphire lasers. *J. Electron Spectrosc. Relat. Phenom.* **2014**, *195*, 231–236. [CrossRef]
24. Gedik, N.; Vishik, I. Photoemission of quantum materials. *Nat. Phys.* **2017**, *13*, 1029–1033. [CrossRef]
25. Jia, C.; Wohlfeld, K.; Wang, Y.; Moritz, B.; Devereaux, T.P. Using RIXS to Uncover Elementary Charge and Spin Excitations. *Phys. Rev. X* **2016**, *6*, 021020. [CrossRef]
26. Mitrano, M.; Wang, Y. Probing light-driven quantum materials with ultrafast resonant inelastic X-ray scattering. *Commun. Phys.* **2020**, *3*, 184. [CrossRef]

27. Zong, A.; Dolgirev, P.; Kogar, A.; Ergeçen, E.; Yilmaz, M.; Bie, Y.; Rohwer, T.; Tung, I.; Straquadine, J.; Wang, X.; et al. Evidence for topological defects in a photoinduced phase transition. *Nat. Phys.* **2019**, *15*, 27–31.
28. Frohlich, H. Electrons in lattice fields. *Adv. Phys.* **1954**, *3*, 325. [CrossRef]
29. Salje, E.K.H.; Alexandrov, A.S.; Liang, W.Y. *Polarons and Bipolarons in High Temperature Superconductors and Related Materials*; Cambridge University Press: Cambridge, UK, 1995. [CrossRef]
30. Franchini, C.; Reticcioli, M.; Setvin, M.; Diebold, U. Polarons in materials. *Nat. Rev. Mater.* **2021**, *6*, 560–586. [CrossRef]
31. Adams, C.P.; Lynn, J.W.; Mukovskii, Y.M.; Arsenov, A.A.; Shulyatev, D.A. Charge Ordering and Polaron Formation in the Magnetoresistive Oxide $La_{0.7}Ca_{0.3}MnO_3$. *Phys. Rev. Lett.* **2000**, *85*, 3954. [CrossRef] [PubMed]
32. Bradley, O.; Batrouni, G.; Scalettar, R. Superconductivity and charge density wave order in the two-dimensional Holstein model. *Phys. Rev. B* **2021**, *103*, 235104. [CrossRef]
33. Chen, C.W.; Choe, J.; Morosan, E. Charge density waves in strongly correlated electron systems. *Rep. Prog. Phys.* **2016**, *79*, 084505. [CrossRef] [PubMed]
34. Bakshi, S.S.; Bose, D.; Dutta, A.; Majumdar, P. Nonequilibrium Dynamics of Suppression, Revival, and Loss of Charge Order in a Laser-Pumped Electron-Phonon System. *Phys. Rev. B* **2024**, *110*, 075102. [CrossRef]
35. Yang, L.; Yang, Y.; Chern, G.W. Pattern Formation in Charge Density Wave States after a Quantum Quench. *Phys. Rev. B* **2024**, *109*, 195133. [CrossRef]
36. Yang, L.; Chern, G.W. Photoinduced Pattern Formation and Melting of Charge Density Wave Order. *Phys. Rev. B* **2025**, *111*, 094208. [CrossRef]
37. Yang, L.; Jang, H.; Bakshi, S.S.; Yang, Y.; Chern, G.W. Pseudospin Formulation of Quench Dynamics in the Semiclassical Holstein Model. *arXiv* **2026**, arXiv:2601.01694. [CrossRef]
38. Jang, H.; Chern, G.W. Suppressed Coarsening After an Interaction Quench in the Holstein Chain. *arXiv* **2026**, arXiv:2602.05815. [CrossRef]
39. Cheng, C.; Zhang, S.; Chern, G.W. Machine Learning for Phase Ordering Dynamics of Charge Density Waves. *Phys. Rev. B* **2023**, *108*, 014301. [CrossRef]
40. Yang, Y.; Cheng, C.; Fan, Y.; Chern, G.W. Enhanced Coarsening of Charge Density Waves Induced by Electron Correlation: Machine-Learning Enabled Large-Scale Dynamical Simulations. *arXiv* **2024**, arXiv:2412.21072. [CrossRef]
41. Bakshi, S.S.; Fan, Y.; Chern, G.W. Machine Learning Modeling of Charge-Density-Wave Recovery After Laser Melting. *arXiv* **2026**, arXiv:2602.03761. [CrossRef]
42. Zwanzig, R. *Nonequilibrium Statistical Mechanics*; Oxford University Press: Oxford, UK, 2001.
43. van Kampen, N.G. *Stochastic Processes in Physics and Chemistry*, 3rd ed.; North-Holland: Amsterdam, The Netherlands, 2007.
44. Gardiner, C.W. *Stochastic Methods: A Handbook for the Natural and Social Sciences*, 4th ed.; Springer: Berlin, Germany, 2009.
45. Kubo, R. The Fluctuation-Dissipation Theorem. *Rep. Prog. Phys.* **1966**, *29*, 255–284. [CrossRef]
46. Caldeira, A.O.; Leggett, A.J. Path Integral Approach to Quantum Brownian Motion. *Phys. A* **1983**, *121*, 587–616. [CrossRef]
47. Bhattacharjee, J.K.; Banerjee, D. *Intermediate Statistical Mechanics*; World Scientific: Singapore, 2016. [CrossRef]
48. Bhattacharyya, S.; Bakshi, S.S.; Kadge, S.; Majumdar, P. Langevin Approach to Lattice Dynamics in a Charge-Ordered Polaronic System. *Phys. Rev. B* **2019**, *99*, 165150. [CrossRef]
49. Bhattacharyya, S.; Bakshi, S.S.; Pradhan, S.; Majumdar, P. Strongly Anharmonic Collective Modes in a Coupled Electron-Phonon-Spin Problem. *Phys. Rev. B* **2020**, *101*, 125130. [CrossRef]

Disclaimer/Publisher's Note: The statements, opinions and data contained in all publications are solely those of the individual author(s) and contributor(s) and not of MDPI and/or the editor(s). MDPI and/or the editor(s) disclaim responsibility for any injury to people or property resulting from any ideas, methods, instructions or products referred to in the content.